



# Multi-resolution open-top light-sheet microscopy to enable efficient 3D pathology workflows

LINDSEY A. BARNER,<sup>1,4</sup> ADAM K. GLASER,<sup>1</sup>  HONGYI HUANG,<sup>2</sup>  
LAWRENCE D. TRUE,<sup>2</sup> AND JONATHAN T. C. LIU<sup>1,2,3,5</sup> 

<sup>1</sup>Department of Mechanical Engineering, University of Washington, Seattle, WA 98195, USA

<sup>2</sup>Department of Laboratory Medicine & Pathology, University of Washington, Seattle, WA 98195, USA

<sup>3</sup>Department of Bioengineering, University of Washington, Seattle, WA 98195, USA

<sup>4</sup>lbarn@uw.edu

<sup>5</sup>jonliu@uw.edu

**Abstract:** Open-top light-sheet (OTLS) microscopes have been developed for user-friendly and versatile high-throughput 3D microscopy of thick specimens. As with all imaging modalities, spatial resolution trades off with imaging and analysis times. A hierarchical multi-scale imaging workflow would therefore be of value for many volumetric microscopy applications. We describe a compact multi-resolution OTLS microscope, enabled by a novel solid immersion meniscus lens (SIMlens), which allows users to rapidly transition between air-based objectives for low- and high-resolution 3D imaging. We demonstrate the utility of this system by showcasing an efficient 3D analysis workflow for a diagnostic pathology application.

© 2020 Optical Society of America under the terms of the [OSA Open Access Publishing Agreement](#)

## 1. Introduction

In recent decades, light-sheet fluorescence microscopy (LSFM) has rapidly risen in popularity as a tool for three-dimensional (3D) and time-lapse (4D) imaging of biological specimens. LSFM combines optically efficient planar illumination with rapid camera-based acquisition, yielding unprecedented imaging speeds with minimal photobleaching and phototoxicity compared to traditional point- or line-scanned volumetric microscopy techniques [1,2]. In addition to gaining traction for biological research, LSFM is now being explored for clinical diagnostic applications [3–5].

Early LSFM microscopy systems, also known as selective plane illumination microscopy (SPIM), were used for imaging small model organisms in which samples were typically embedded in agarose and placed within cuvettes or capillary tubes [6,7]. Variants such as ultramicroscopy and inverted selective plane illumination microscopy (iSPIM) later emerged for applications involving larger specimens, but still imposed geometric constraints due to bulky objectives being positioned to the side or above the samples [8,9]. To address some of these sample-mounting and size limitations [10–13], we and others have developed open-top light-sheet (OTLS) microscopes as versatile, easy-to-use platforms for imaging cleared tissues of arbitrary size and number [3,5,14–17].

In OTLS microscopy, cleared specimens are simply placed on a flat, transparent sample holder and imaged from below, similar to how a document is placed and imaged on a flatbed scanner. The physical space above the sample holder is unconstrained, enabling specimens of nearly any size, shape, or quantity to be imaged up to a certain depth (typically several millimeters in optically cleared specimens) [18]. Below the sample holder, the illumination and collection axes are oriented at 45° angles with respect to the vertical axis. This geometry requires careful refractive index and/or wavefront matching to suppress off-axis aberrations as the beams transition at an oblique angle between media with different refractive indices (e.g. sample holder, immersion oil,

specimen, air, etc.). As illustrated in Fig. 1, early implementations of OTLS used a water-filled prism or solid immersion lens (SIL) to provide an approximately normal interface for the focusing beams as they transition between air and a higher-index medium. This minimizes aberrations, but prohibits vertical motion of the sample and therefore deeper imaging in the case of a SIL [3,5,14]. Alternatively, our most-recent implementation of OTLS employs a multi-immersion collection objective dipped within an immersion chamber (Fig. 1(c)), which enables vertical motion of the sample [16]. Note that for all of these designs, it is critical that the refractive index of the immersion liquid, sample holder, and specimen are closely matched to allow for aberration-free imaging [16].

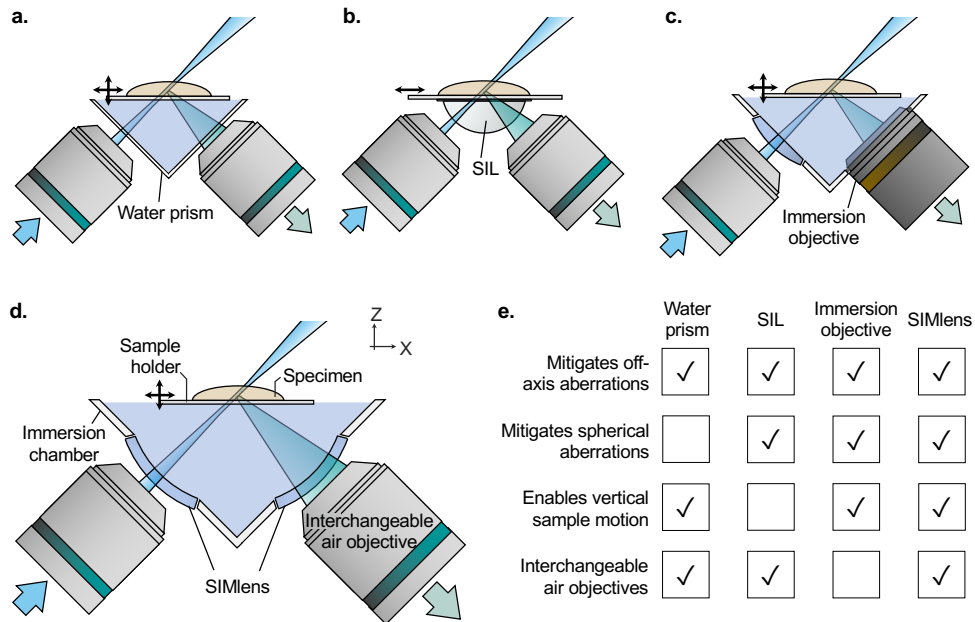


**Fig. 1.** To minimize aberrations as optical rays transition across a  $45^\circ$  angled interface in OTLS microscopy, the first implementation of OTLS utilized a (a) water-filled glass prism [14] to reduce off-axis (but not spherical) aberrations. Subsequent implementations utilized (b) a solid immersion lens (SIL) [3,5], which mitigates off-axis and spherical aberrations but prohibits vertical sample motion, or (c) an immersion objective [16], which circumvents aberrations but makes it difficult to change objectives. (d) Presented here, the development of a solid immersion meniscus lens (SIMlens) prevents off-axis and spherical aberrations and enables the use of air-based objectives that may be interchanged for multi-resolution OTLS microscopy [19]. (e) Comparison of wavefront-matching strategies implemented in OTLS microscopy.

As with any imaging technique, the imaging durations, analysis times, and dataset sizes scale with resolution (to the third power for volumetric imaging). For example, for LSFM imaging with sub-micron resolution (assumed to be isotropic in this simplified example), large tissue volumes can require hours or even days to image with state-of-the-art sCMOS cameras ( $<0.25 \text{ mm}^3/\text{min}$  for  $0.5\text{-}\mu\text{m}$  resolution) in cases that are camera-limited and not photon-limited (where the latter condition would necessitate even longer imaging times).

Unfortunately, previous OTLS microscope designs have not been ideal for multi-resolution imaging (Fig. 1(c)) [16]. To overcome this, we have designed a solid immersion meniscus lens (SIMlens) concept, which is a wavefront-matching element for focused beams as they transition between various media with disparate refractive indices [19]. Here, we show that

our SIMlens concept enables the use of readily available and inexpensive air-based objectives for OTLS microscopy (as shown in Fig. 1(d)), in which the air-based objectives can be easily interchanged with a motorized turret. We describe the optical and mechanical design of this first-ever multi-resolution OTLS microscope, along with its imaging performance for low- and high-resolution views of thick, intact, optically clear tissues. To maximize its versatility for clinical and laboratory settings, this system is the most-compact OTLS system to date, measuring approximately  $1 \times 2 \times 1$  ft ( $30.5 \times 61.0 \times 30.5$  cm) in length, width, and height. While the benefits of OTLS microscopy for user-friendly imaging of large and diverse specimens have already been demonstrated, this portable multi-resolution OTLS system will further facilitate the adoption of OTLS microscopy for time- and data-efficient investigations and diagnostics involving large specimens. To practically illustrate these advantages, an example multi-resolution 3D pathology workflow is demonstrated for human prostate carcinoma specimens.

## 2. Methods

### 2.1. Main body design

Air-based illumination and collection objectives are positioned orthogonal to one another, outside an immersion chamber, and each at a  $45^\circ$  angle relative to the vertical axis (Fig. 2(a)). Prior to the air objectives, the respective illumination and collection optics are mounted on breadboards ( $5'' \times 12''$  and  $4'' \times 24''$ ) that are also positioned at a  $45^\circ$  angle relative to the optical table (Fig. 2(a)). On the distal side of the air objectives, a pair of SIMlenses (custom fabricated by BMV Optical Technologies for \$700/each) are precisely aligned to enable wavefront matching of the focused beams as they transition between air and a higher-index immersion liquid (see section 2.2 and Fig. 3 for details). The SIMlenses are mounted at the interface of a liquid-filled immersion chamber. Above the immersion chamber, a modular sample holder is mounted on a motorized XYZ translation stage (Applied Scientific Instrumentation MS2000, LS-100). The entire OTLS system fits on a  $1' \times 2'$  breadboard (Thorlabs, MB1224) and can be installed on a portable optical cart (Thorlabs, POC001).

### 2.2. SIMlens design

We designed a solid immersion meniscus lens (SIMlens) to enable wavefront matching of illumination and collection rays as they transition from air-based objectives into the high-index medium contained within an immersion chamber. Our SIMlens features two spherical meniscus surfaces, both of which have a center of curvature that is aligned precisely to the focal point of its accompanying air-based objective, as shown in Fig. 3. Rays converging to the focal point are oriented normal to the SIMlens surfaces, enabling them to travel from the air-based objective into the higher-index medium of the immersion chamber (or vice versa) without encountering refractive aberrations. This design has several advantages. (1) A SIMlens, which is relatively low-cost to custom manufacture ( $\sim \$700/\text{each}$ ), enables the use of air-based objectives which are inexpensive and readily available compared to specialized immersion-based objectives. Additionally, air-based objectives permit the implementation of a turret, on which multiple objectives may be installed for multi-resolution imaging. This would not be feasible in immersion-objective-based OTLS architectures (Fig. 1(c)) since the objectives cannot be changed without first evacuating the immersion chamber [16]. (2) The SIMlens is compatible with any immersion liquid or clearing protocol (assuming precise refractive index matching to the sample and sample holder). Since the SIMlens surface adjacent to the immersion media performs wavefront matching (i.e. the interface is perpendicular to focusing rays), index matching of the SIMlens and immersion medium is not necessary. Therefore the immersion medium can be any refractive index, provided it is matched to that of the sample and sample holder. (3) A SIMlens provides an increase in the NA and magnification of the air-based objective, by a factor of the immersion medium refractive index,  $n$ .

Since rays do not change angle ( $\theta$ ) as they transition through the SIMlens into the high-index immersion medium ( $n$ ), the NA increases according to  $NA = n \times \sin \theta$ .

The SIMlenses on the illumination and collection side are identical ( $R_1 = 15.5$  mm,  $R_2 = 17$  mm, as shown in Fig. 3) and were custom-fabricated by BMV Optical Technologies. In order to maximize the wavefront-matching performance across the field of view (FOV), the SIMlens radii were designed to be as large as possible without exceeding the working distance (WD) of the objectives (20X WD = 19 mm, 5X WD = 23 mm). Since rays emerging from the edges rather than the center of the FOV are not perfectly normal to the SIMlens surface, a large SIMlens radius relative to the FOV at the focal plane ensures that all rays transition through the SIMlens interfaces at approximately normal angles, where refraction is minimized. Ray-tracing simulations (ZEMAX) demonstrate that diffraction-limited performance is achieved (i.e. a Strehl ratio  $> 0.80$ ) across the FOV when the SIMlens is paired with the 5X and 20X objectives, as shown in Fig. 3(b). Perfect index matching among the immersion media, sample plate, and sample are assumed for cases including  $n = 1.33$ , 1.49, and 1.56 (where FEP film, PMMA, and

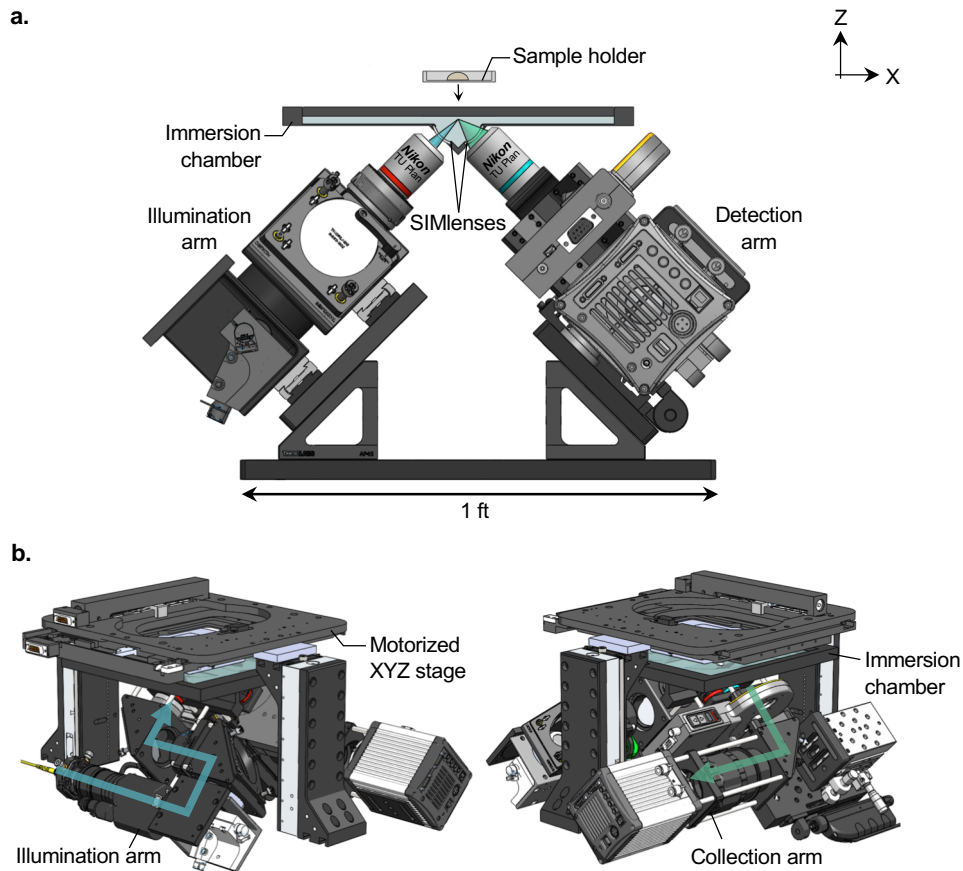


**Fig. 2.** Mechanical design schematics of the multi-resolution OTLS microscope. (a) Side view of the microscope. Illumination and collection arms are installed on breadboards placed at a  $45^\circ$  angle relative to the vertical axis. Specimens of any size or shape may be placed on a modular sample holder, which is then mounted to a motorized XYZ stage. (b) Isometric views of the microscope showing the illumination arm (left) and collection arm (right). Direction of respective beam paths are shown.

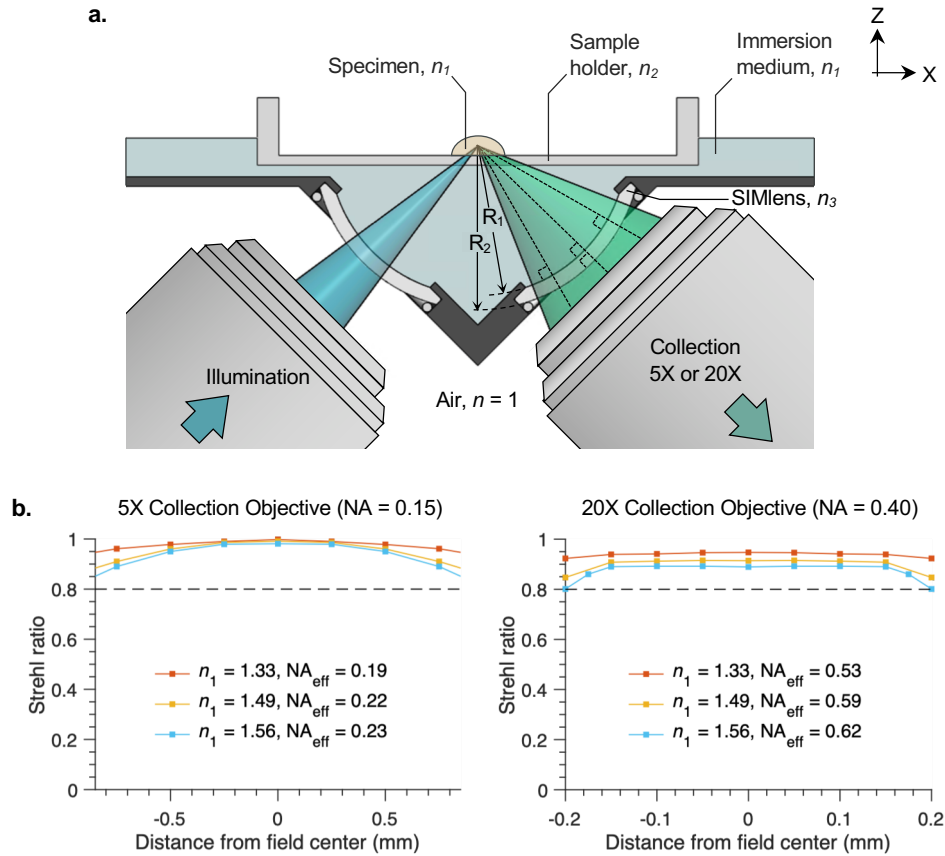


**Fig. 3.** (a) To enable illumination and collection beams to transition from air to a high-index immersion medium without encountering refractive aberrations, custom SIMlenses are precisely positioned in front of air-based objectives at the interface of the immersion chamber. The radii of curvature of both surfaces ( $R_1 = 15.5$  mm,  $R_2 = 17$  mm) of a SIMlens coincide with the focal point of its corresponding objective. To seal the SIMlens at the periphery of the immersion chamber, an O-ring gasket is held in place by a retaining ring (not shown) behind the SIMlens. Note that to achieve diffraction-limited performance, the refractive index of the sample holder ( $n_2$ ) must be precisely matched to that of the immersion medium ( $n_1$ ). (b) Strehl ratios, based on ray-trace simulations, are shown across the FOV of both a 5X objective (left plot) and 20X objective (right plot) when used in conjunction with the custom-machined SIMlens. The Strehl ratio is shown for various immersion-medium refractive indices ( $n_1$ ), which is assumed to match  $n_2$ . Both objectives achieve diffraction-limited imaging (defined here as a Strehl ratio  $> 0.80$ , which is indicated by the dashed line) within their FOV for immersion-medium indices ranging from  $n_1 = 1.33 - 1.56$ .

Hivex [16] may be used as index-matching sample holders in each respective case). Note that the FOV in this case is defined by the size of the camera chip (2048 pixels) and sampling pitch, rather than the FOV of the objective, which is larger. The SIMlens is mounted and sealed at the periphery of the immersion chamber with an off-the-shelf O-ring gasket (The O-Ring Store, Buna-N 70 JIS S16) and retaining ring (Thorlabs, SM19RR), in which the O-ring is robust to a wide range of solvents including ethyl cinnamate (ECi).



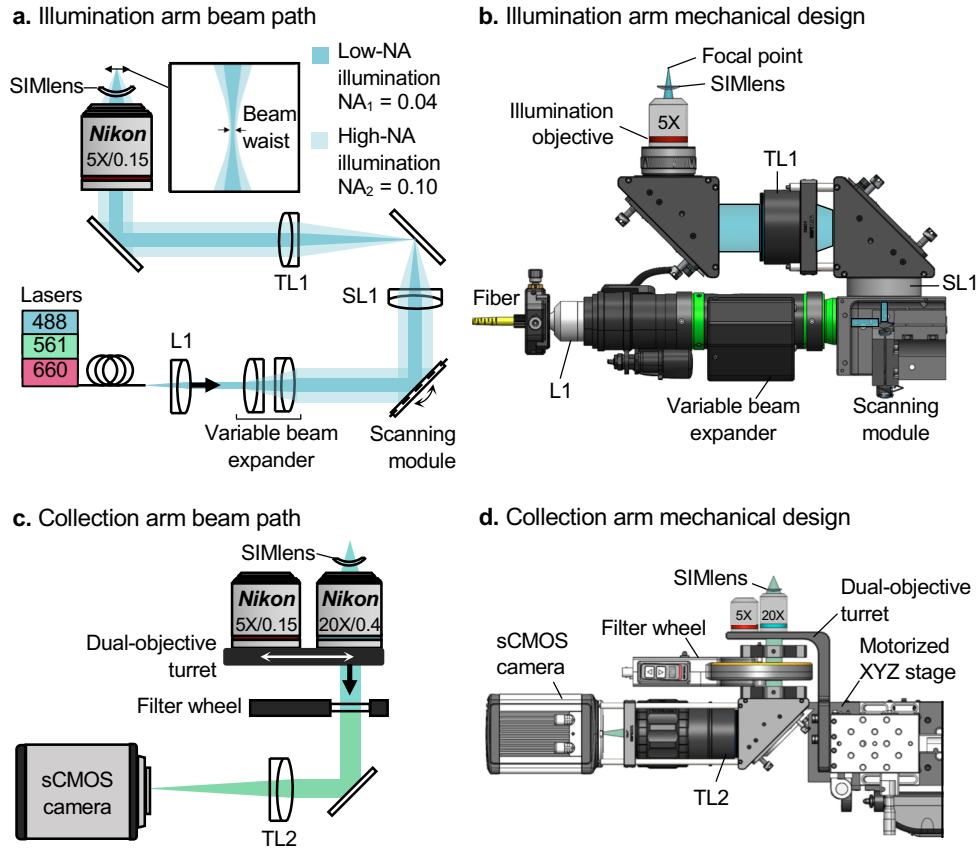


**Fig. 4.** (a) Schematic of the illumination arm beam path for both low- and high-NA illumination. (b) Illumination arm CAD. Custom mounting components include the dual-axis galvanometer mount and adapter for SL1 (Hilltop Technology Laboratory, Inc.). (c) Schematic of the beam path for high-NA collection. (d) Collection arm CAD. Custom components include the dual-objective turret and an adapter for the motorized XYZ stage (machined by Hilltop Technology Laboratory, Inc.)

### 2.3. Illumination and collection arms

On the illumination arm, Gaussian illumination is delivered through a single-mode fiber (Thorlabs RGB50HA,  $NA = 0.12$ ,  $\lambda = 488, 561, 660$  nm) and is collimated by a 20X objective (Nikon MUL04201,  $f = 10$  mm). A motorized zoom module (Qioptiq FUSION 7:1 Stepper) expands and re-collimates the beam, which enables the light sheet NA to be adjusted to provide a relatively uniform (i.e. within the Rayleigh range) light-sheet thickness across the imaged FOV [20] for both low- and high-resolution imaging modes. A pair of orthogonal galvanometric scanning mirrors (“scanning module” in Fig. 4) is located at a conjugate back focal plane; one mirror scans the point-focused Gaussian beam across the field of view (as a digitally scanned light sheet) [21], whereas the other mirror is used to align the light sheet along the axial direction of the collection path. The beam is then relayed by a scan lens (Thorlabs LSM03-VIS,  $f = 39$  mm) and tube lens (Thorlabs TTL100-A,  $f = 100$  mm) to the back focal plane of a 5X objective (Nikon CFI TU Plan Fluor EPI,  $f = 40$  mm). The focusing beam then transitions through the custom-fabricated SIMlens ( $R_1 = 15.5$  mm,  $R_2 = 17$  mm) into the immersion chamber, and then passes through the sample holder into the specimen. For low-resolution imaging, the effective NA of the light

sheet is  $NA_1 \sim 0.04$  with a  $\sim 5.9\text{-}\mu\text{m}$  thickness (FWHM) and  $240\text{-}\mu\text{m}$  depth-of-focus (DOF). For high-resolution imaging, the effective NA of the light sheet is  $NA_2 \sim 0.10$  with a  $\sim 2.75\text{-}\mu\text{m}$  thickness (FWHM) and  $50\text{-}\mu\text{m}$  DOF.

On the collection arm, two air-based collection objectives (5X Nikon CFI TU Plan Fluor,  $NA = 0.15$  and 20X Nikon CFI TU Plan ELWD,  $NA = 0.40$ ) are implemented on a motorized linear stage (Newport 436, LTA-HS) that automates the switching between imaging modes. After fluorescence travels through the SIMlens and collection objective (5X or 20X), it is filtered by a motorized filter wheel (Thorlabs FW102C). Band-pass filters are used for the detection of fluorescence excited at one of three wavelengths: 488-nm (Semrock FF01-496/LP-25), 561-nm (Semrock, BLP02-561R-25), and 660-nm (Semrock LP02-664RU-25). Finally, fluorescence is imaged by a tube lens (Thorlabs TTL200-A,  $f = 200\text{mm}$ ) onto a sCMOS camera (Hamamatsu ORCA-Flash4.0 V2). When ethyl cinnamate (ECi) is used as an immersion medium ( $n_1 = 1.56$ ), the 5X objective provides  $\sim 1.70\text{ }\mu\text{m}$  lateral resolution (FOV  $\sim 1.75\text{ mm}$ ), whereas the 20X objective provides  $\sim 0.6\text{ }\mu\text{m}$  lateral resolution ( $\sim 0.40\text{ mm}$  FOV). Note that these lateral-resolution metrics refer to the FWHM dimension of the collection PSF. The actual sampling pitch at the camera is  $0.83\text{ }\mu\text{m/px}$  and  $0.21\text{ }\mu\text{m/px}$ , respectively (slightly better than Nyquist sampling in both cases). The axial resolution of the system is defined by the thickness of the light sheet, which is  $5.89\text{ }\mu\text{m}$  and  $2.75\text{ }\mu\text{m}$  (FWHM) for low- and high-resolution imaging, respectively. Beam-path schematics and computer-aided design (CAD) renderings of the illumination and collection arms are shown in Fig. 4.

#### 2.4. Sample holder and stage scanning

For sample mounting, a modular transparent holder is suspended below a motorized XYZ stage (Applied Scientific Instrumentation MS2000, LS-100). Optically cleared specimens, such as those treated with CLARITY, CUBIC, or organic solvent-based protocols such as iDISCO [22–24], are simply placed on the top surface of the holder which is dipped into the immersion liquid. During imaging, the holder is stage-scanned through the light sheet in three dimensions (XYZ) to create a series of volumetric image strips, which are tiled to create a large volumetric image of the specimen (as described in previous publications) [3,16]. The scanning and imaging processes are entirely controlled via a Python script, derived from open-source packages and device drivers available on GitHub [25]. Imaging data is compressed by  $\sim 10\text{X}$  using B3D compression [26] and stored as 3D datasets in the hierarchical data format (HDF5), which can be interactively viewed in BigStitcher [27]. Volumetric imaging is achieved at a maximum rate of  $10\text{ mm}^3/\text{min}$  in the low-resolution mode, and  $0.13\text{ mm}^3/\text{min}$  in the high-resolution mode if B3D compression is not performed. With B3D compression, low- and high-resolution imaging rates are  $2.5\text{ mm}^3/\text{min}$  and  $0.03\text{ mm}^3/\text{min}$ , respectively, due to the speed limitations of the B3D program when running on our system which employs a NVIDIA TITAN Xp graphics card with CUDA 10.2.

As mentioned, precise index matching between the sample holder, immersion medium, and specimen is required for aberration-free imaging. Based on ray-tracing analyses (section 3.1), sample-holder materials and thicknesses were chosen to ensure diffraction-limited imaging performance for the chosen clearing protocol(s). For example, for ECi-based clearing [18], a HIVEX ( $n_2 = 1.56$ ) sample holder with a thickness of  $150\text{ }\mu\text{m}$  (custom-machined by BMV Optical Technologies) can be used. Alternatively,  $13\text{-}\mu\text{m}$  thick off-the-shelf polyetherimide (PEI,  $n_2 = 1.69$  PolyK Technologies, LLC) films may be used for small or lightweight samples. Both options achieve near-diffraction-limited imaging (Strehl ratio  $> 0.80$ ) for NAs of up to 0.625 according to ZEMAX simulations.

### 3. Results

#### 3.1. Zemax simulations

Ray-tracing simulations (ZEMAX) were implemented to characterize device performance. In models of the illumination arm, the initial element is a collimated Gaussian beam located at the scanning module. The diameter of this collimated beam is determined by the NA of the fiber source ( $\text{NA} \sim 0.12$ ), focal length of the collimating objective ( $f = 10$  mm), and magnification setting of the variable beam expander (range 0.35–2.48X), which is used to adjust the beam for the two imaging modes. For low-NA imaging, the Gaussian beam diameter is 0.84 mm ( $1/e^2$ ). The corresponding diameter for high-NA imaging is 2.80 mm. The scanning module is followed by a scan lens (Thorlabs LSM03-VIS,  $f = 39$  mm) and tube lens (Thorlabs TTL100-A,  $f = 100$  mm), which are modeled in ZEMAX as “black box” modules obtained from Thorlabs. Finally, the tube lens is followed by a kinematic mirror, objective (JPO patent JPH11231224), and SIMlens. Spot diagrams of the point-focused Gaussian beam across the FOV indicate that aberrations are minimal for the low- and high-NA light sheets (shown in Fig. 5).

Ray-tracing simulations were also used to characterize performance of the collection arm, as shown in Fig. 6 (high-resolution mode only, which is more sensitive to aberrations). A long-working-distance 20X objective ( $\text{NA} = 0.40$ ,  $f = 10$  mm US Patent 7848027B2) was paired with a SIMlens and tube lens ( $f = 200$  mm, Thorlabs TTL200-A). A flat interface, angled at  $45^\circ$  relative to the optical axis, was modeled with various refractive indices and thicknesses ( $t$ ) to examine the optical tolerance to refractive-index mismatch ( $\Delta n$ ) between the sample holder and immersion medium. As has been quantified with previous immersion-based OTLS systems [16], the Strehl ratio was assessed as a function of optical path difference ( $\Delta n \times t$ ) and NA to determine the maximum allowable optical path difference for diffraction-limited imaging. Additionally, the Huygens method in ZEMAX was implemented to simulate point spread functions (PSF).

#### 3.2. Characterization of device performance

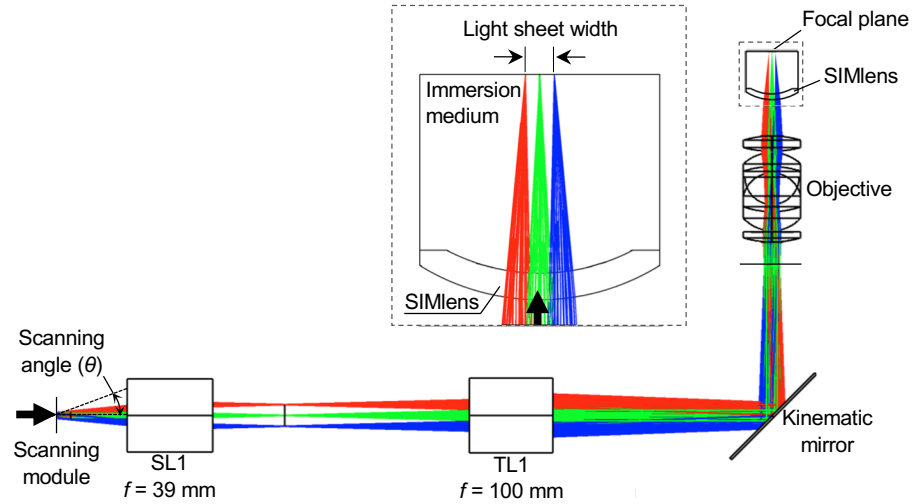
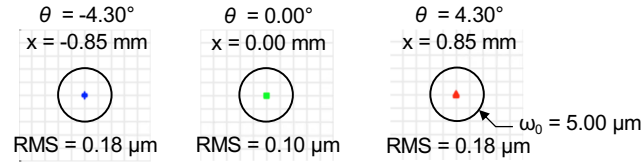
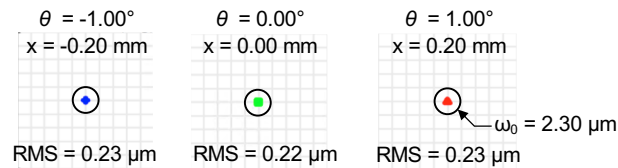
To experimentally assess the system's performance in low- and high-resolution imaging modes, sub-diffraction-limited beads were imaged in three dimensions as shown in Fig. 7. Agarose phantoms (1% w/v) were embedded with a uniform distribution of gold nanoparticles (175 nm diameter), cleared in ethyl cinnamate (ECi), and placed on a 150- $\mu\text{m}$  thick HIVEX sample holder for imaging in an ECi-based immersion bath. Beads were illuminated at 660 nm and imaged in reflectance with both the 5X and 20X objective. Point spread functions (PSF) were averaged among  $n = 5$  beads. The full-width at half maximum (FWHM) intensity profile at 5X was measured to be 1.74  $\mu\text{m}$  in the Y direction, 2.56  $\mu\text{m}$  in the X direction, and 2.51  $\mu\text{m}$  in the Z (vertical) direction, as is shown in Fig. 7(a) (coordinate axes shown in Fig. 3). As displayed in Fig. 7(b), the FWHM at 20X was measured to be 0.68  $\mu\text{m}$  in the Y direction, 1.09 in the X direction, and 1.07  $\mu\text{m}$  in the Z direction. Note that the worst dimension of the PSF is along the collection axis (“axial” direction). This is determined by the thickness of the illumination light sheet, which is 5.89  $\mu\text{m}$  and 2.75  $\mu\text{m}$  (FWHM) for low- and high-resolution imaging modes, respectively. Note that the term “vertical” is defined with respect to the gravitational axis here.

#### 3.3. Multi-resolution imaging of human prostate carcinoma

In experimental or clinical practice, multi-resolution workflows are common, in which only localized regions of interest are imaged/visualized at the highest levels of resolution. In conventional histopathology, >90% of tissues are surveyed only at low resolution (with 5X to 10X objectives) to rapidly identify suspicious or ambiguous structures. This enables large fields of view to be examined quickly, which is important for tissues/diseases that are spatially heterogeneous and large in extent. In select cases, suspicious or ambiguous regions are then imaged at higher resolution (typically with 20X to 40X objectives) [28–31].



## a. Ray tracing of illumination arm

b. Spot diagrams across FOV ( $NA_1 = 0.04$ )c. Spot diagrams across FOV ( $NA_2 = 0.10$ )

**Fig. 5.** (a) To create a digitally-scanned light sheet at the focal plane over time, a mirror scans a Gaussian pencil beam laterally before the beam passes through a scan lens (SL1), tube lens (TL1), objective, and SIMlens. ZEMAX simulations were used to assess spot diagrams of the illumination beam at different points across the FOV. Spot diagrams are shown for different points across the FOV for (b) low-resolution ( $NA_1$ ) and (c) high-resolution ( $NA_2$ ) illumination. Note that the black circles in (b) and (c) refer to the size of an ideal Gaussian focus with a  $1/e^2$  beam waist radius of  $\omega_0$ . The spread in the spot diagram is minimal compared to the size of an ideal Gaussian focus, which suggests that the optical performance is near the diffraction limit. “RMS” refers to the root-mean-squared spread in the spot diagrams as shown.

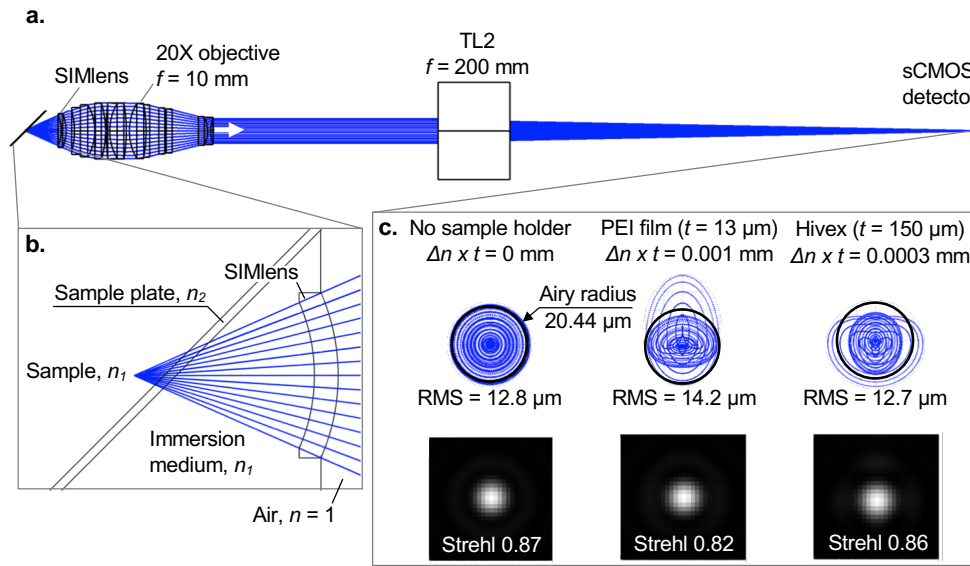
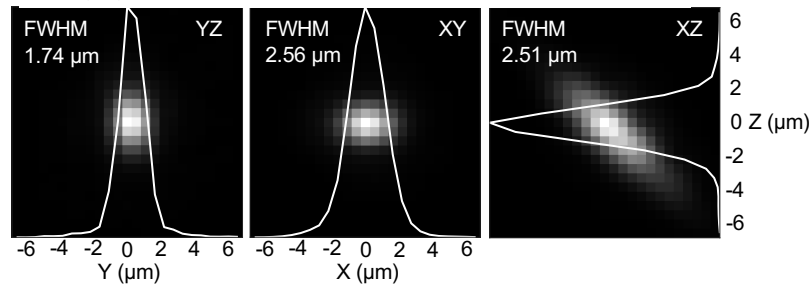


**Fig. 6.** (a) In the ZEMAX model of the high-NA collection arm, uniform fluorescence originates at the sample ( $n_1$ ) and traverses through an angled sample holder ( $n_2$ ), immersion medium ( $n_1$ ), and SIMlens before entering the 20X air-based objective. Then, the fluorescence transmits through a tube lens ( $f = 200$  mm) onto a camera (image plane). (b) Enlarged view of the focal region, sample holder (thickness  $t$ ), and SIMlens.  $\Delta n = n_1 - n_2$  is the refractive index mismatch between the immersion media and sample holder, where ideally  $\Delta n = 0$ . (c) Simulations of the system's spot diagram (top) and PSF (bottom) with an ethyl cinnamate clearing medium (ECi,  $n_1 = 1.56$ ) and various sample holders are shown. The black circle in the spot diagrams indicates the Airy disk for a uniform beam that is ideally imaged onto the detector plane. The left plot shows simulations with no sample holder ( $\Delta n = 0$ ). The middle and right plots show that when a PEI film ( $n_2 = 1.69$ , 13  $\mu\text{m}$  thick) or Hivex substrate ( $n_2 = 1.56$ , 150  $\mu\text{m}$  thick) is used with the ECi clearing medium, they both lead to acceptable imaging performance (Strehl ratio  $> 0.80$ ). "RMS" refers to the root-mean-squared spread in the spot diagrams as shown.

We demonstrate the efficiency of this multi-resolution OTLS imaging workflow for the initial identification and then definitive diagnosis of prostate cancer in radical prostatectomy specimens. Slices of fixed prostate tissue (2-3 mm thick) were stained with a fluorescent analog of H&E (TO-PRO 3 and eosin), cleared in ECi ( $n_1 = 1.56$ ) [18], and placed on a flat HIVEX sample holder ( $n_2 = 1.56$ , thickness = 150  $\mu\text{m}$ ) for multi-resolution OTLS microscopy [16]. Tissue slices (approximately 30 mm<sup>3</sup> in volume) were first rapidly imaged with the 5X objective (at a volumetric imaging rate of 2.5 mm<sup>3</sup>/min; see section 2.4 for more details). The dataset was immediately viewed in BigStitcher with minimal post-processing to identify regions of diagnostic importance and/or ambiguity. In Fig. 8, low resolution images that appear to contain tumor infiltrating lymphocytes, blood vessels, and clusters of small glands (potentially carcinoma) are shown. These structures were then imaged in the high-resolution mode to confirm their identity (including diagnosis of the glands). High-resolution imaging is able to resolve flattened endothelial cells that confirm the presence of blood vessels. Additionally, a single layer of epithelial cells with large nucleoli is seen lining the lumen of the small glands, which indicates that these glands are cancerous (lacking a basal cell layer) [29]. Note that the images shown in

## a. 5X imaging point spread function



## b. 20X imaging point spread function

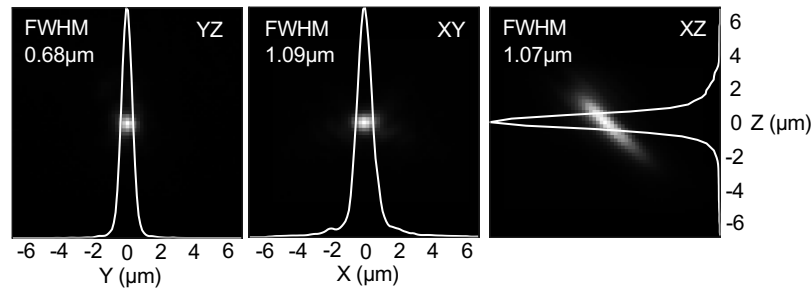


**Fig. 7.** Intensity point spread functions (PSFs) obtained by imaging sub-diffraction limited beads in ECI ( $n_1 = 1.56$ ) at (a) 5X ( $NA_{\text{eff}} = 0.23$ ) and (b) 20X ( $NA_{\text{eff}} = 0.62$ ). Line profiles of the PSFs in the X, Y, and Z directions are used to characterize the resolution of the system. (a) At 5X, the FWHM is  $1.74 \mu\text{m}$  in the Y direction,  $2.56 \mu\text{m}$  in the X direction, and  $2.51 \mu\text{m}$  in the Z direction. (b) At 20X ( $NA_{\text{eff}} = 0.62$ ), the FWHM was measured to be  $0.68 \mu\text{m}$  in the Y direction,  $1.09 \mu\text{m}$  in the X direction, and  $1.07 \mu\text{m}$  in the Z direction.

Fig. 8 were post-processed with a Beer-Lambert based false-coloring algorithm to mimic the appearance of conventional H&E histology [32,33].

Imaging the example tissue slice shown in Fig. 8 in its entirety at high resolution would require at least 3–4 hours at maximum imaging speed. Imaging at low resolution, however, is achieved in a matter of minutes, from which certain diagnostic features of importance or ambiguity can be identified for subsequent localized high-resolution interrogation. It should be noted that 3D volumetric information allows for comprehensive assessment of tissue architecture in a way that traditional slide-based histology cannot achieve. In certain cases where sampling artifacts are known to occur in 2D histology, 3D assessment can potentially improve diagnostic and prognostic interpretation. For example, the grading of prostate cancer can depend upon visualization of “poorly formed glands,” the most common Gleason pattern (GP) 4 subtype [34]. GP4 indicates a more aggressive carcinoma than lower GP scores, and is often the threshold at which surgery or radiation therapy is recommended as opposed to active surveillance (for GP3 carcinomas) [35]. However, the appearance of “poorly formed glands” can be due to tangential-sectioning artifacts in 2D histology [36], as is demonstrated in Fig. 8(b). In this example, a gland that appears to be poorly formed in a single 2D frame (analogous to traditional slide-based histology) is revealed to be fully formed (GP3 rather than GP4) when viewing other depths in the specimen.

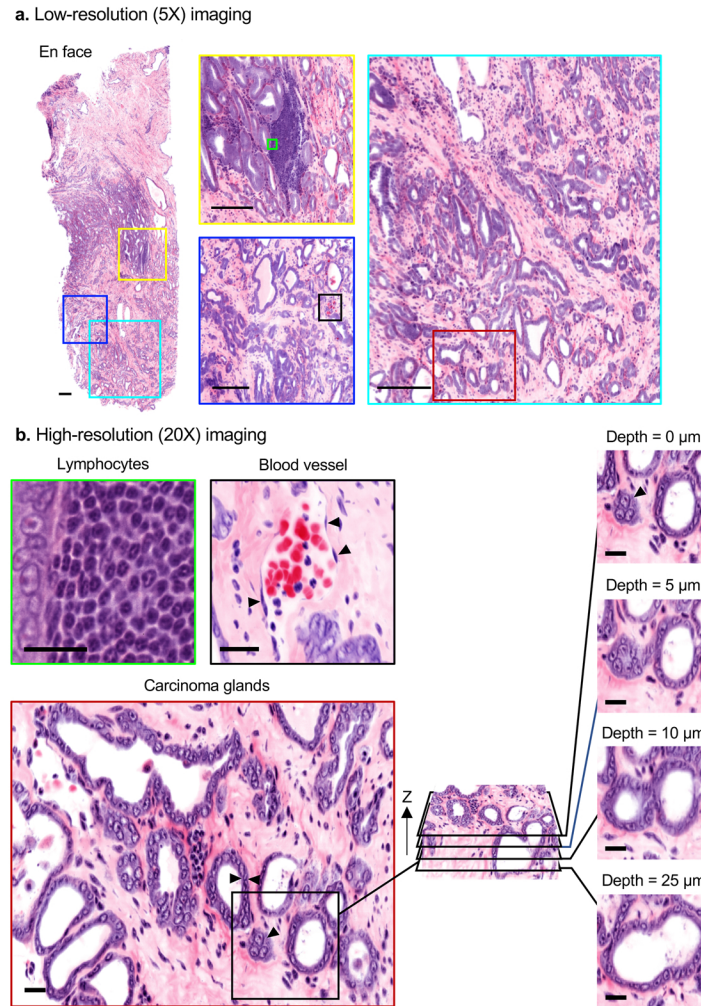


**Fig. 8.** Multi-resolution OTLS imaging of human prostate carcinoma. (a) Low-resolution views of a 2.5-mm-thick slice from a prostatectomy specimen that is fluorescently stained with TO-PRO 3 and eosin, cleared, and then imaged with a 5X air objective. The images are false-colored to mimic the appearance of H&E staining. On the left is an *en face* cross-sectional view of the whole specimen. On the right are regions containing diagnostically important or ambiguous features identified from the low-resolution dataset (at various depths in the specimen). The middle two images appear to contain lymphocytes (green box within yellow box) and a small blood vessel (black box within dark blue box), whereas the image on the right contains many clusters of small glands that appear to be carcinoma (exemplified in the red box within the light blue box). Scale bars represent 200  $\mu\text{m}$ . (b) High-resolution imaging (20X air objective) confirms the identity of these elements. A cluster of lymphocytes is adjacent to carcinoma cells that have large nuclei with prominent nucleoli (top left). Flat endothelial cells of a vessel are seen, adjacent to a small cluster of carcinoma cells (top center). The small glands (bottom left) are lined by a single layer of epithelial cells that have large nucleoli, which is diagnostic of prostate adenocarcinoma (black arrows). To demonstrate the value of 3D information in assessing glandular morphology, which is used to grade the aggressiveness of prostate cancers, a z-stack of images is shown in which a gland appears to be “poorly formed” (Gleason pattern 4) in a single 2D view (black arrow), but is revealed to be a well-formed gland (Gleason pattern 3) when viewing the full 3D dataset (right). Scale bars represent 20  $\mu\text{m}$ .

#### 4. Summary

Here we report development of the first multi-resolution OTLS microscope that employs a novel solid immersion meniscus lens (SIMlens) for wavefront matching of rays from air-based objectives into immersion media of various indices. The system is our most-compact OTLS microscope to date and features two imaging modalities (5X and 20X) that users can rapidly transition between with the aid of a motorized turret of air objectives (collection arm) and a zoom module (illumination arm).

While a systematic comparison is beyond the scope of this paper, we believe that our multi-resolution OTLS microscope has advantages over alternatives such as single-objective light-sheet microscopy (i.e. OPM, SCAPE, SOPi) [10,37,38] and computational tomographic 3D microscopy techniques such as light-field microscopy (LFM) and Fourier ptychographic microscopy (FPM) [39–41]. Multi-resolution imaging with single-objective light-sheet microscopy is possible in principle — either by swapping primary objectives, or by utilizing one “super objective” that has a large field of view, NA, and working distance (where downstream optics may enable switching between imaging modes). However, there is significant complexity in tailoring the illumination and collections beams of single-objective systems, including a tilted remote-focus along the collection arm, to accommodate different imaging modes [42]. Computational 3D microscopy techniques like LFM and FPM can achieve rapid 3D imaging but are often less ideal for imaging deeply within densely labeled specimens due to limitations imposed by background shot-noise and the finite dynamic range of detector arrays. Additionally, in its original and most-popular forms, FPM cannot image incoherent fluorescence contrast.

We anticipate that our technology will enable pathologists to rapidly assess clinical specimens in 3D in a similar manner to standard multi-resolution workflows in histopathology, thus encouraging the translation of OTLS-based nondestructive 3D pathology into clinical settings. Additionally, we expect that multiresolution 3D microscopy will be of value to biologists for identifying specific structures (especially rare/sparse objects) in large heterogeneous specimens. In the future, machine learning algorithms could be trained to recognize structures of interest from low-resolution images and to automatically direct the system to re-image those structures at high resolution, which could greatly expedite clinical diagnostic workflows, including computer-assisted diagnoses.

#### Funding

National Cancer Institute (P50CA097186); U.S. Department of Defense (W81XWH-18-10358); NIH (K99 CA240681, R01CA175391, R01CA244170); National Science Foundation (DGE-1762114).

#### Acknowledgments

The authors would like to thank Jon Daniels (Applied Scientific Instrumentation, Inc.), Chengbo Yin, Kevin Bishop, and Robert Serafin for helpful discussions. LB further acknowledges funding from the ARCS Foundation.

#### Disclosures

A.K.G., L.D.T., and J.T.C.L. are cofounders and shareholders of LightSpeed Microscopy, Inc. (I,E).

#### References

1. E. G. Reynaud, J. Peychl, J. Huiskens, and P. Tomancak, “Guide to light-sheet microscopy for adventurous biologists,” *Nat. Methods* **12**(1), 30–34 (2015).
2. R. M. Power and J. Huiskens, “A guide to light-sheet fluorescence microscopy for multiscale imaging,” *Nat. Methods* **14**(4), 360–373 (2017).



3. A. K. Glaser, N. P. Reder, Y. Chen, E. F. McCarty, C. Yin, L. Wei, Y. Wang, L. D. True, and J. T. C. Liu, "Light-sheet microscopy for slide-free non-destructive pathology of large clinical specimens," *Nat. Biomed. Eng.* **1**(7), 1–10 (2017).
4. B. Hu, D. Bolus, and J. Brown, "Dual-view inverted selective plane illumination microscopy (diSPIM) with improved background rejection for accurate 3D digital pathology," *Proc. SPIE* **9**, 1049 (2018).
5. Y. Chen, W. Xie, A. K. Glaser, N. P. Reder, C. Mao, S. M. Dintzis, J. C. Vaughan, and J. T. C. Liu, "Rapid pathology of lumpectomy margins with open-top light-sheet (OTLS) microscopy," *Biomed. Opt. Express* **10**(3), 1257–1272 (2019).
6. J. Huisken, J. Swoger, F. Del Bene, J. Wittbrodt, and E. H. K. Stelzer, "Optical Sectioning Deep Inside Live Embryos by Selective Plane Illumination Microscopy," *Science* **305**(5686), 1007–1009 (2004).
7. R. Tomer, K. Khairy, F. Amat, and P. J. Keller, "Quantitative high-speed imaging of entire developing embryos with simultaneous multiview light-sheet microscopy," *Nat. Methods* **9**(7), 755–763 (2012).
8. H. U. Dodt, U. Leischner, A. Schierloh, N. Jähring, C. P. Mauch, K. Deininger, J. M. Deussing, M. Eder, W. Ziegler, and K. Becker, "Ultramicroscopy: Three-dimensional visualization of neuronal networks in the whole mouse brain," *Nat. Methods* **4**(4), 331–336 (2007).
9. Y. Wu, A. Ghitani, R. Christensen, A. Santella, Z. Du, G. Rondeau, Z. Bao, D. Colón-Ramos, and H. Shroff, "Inverted selective plane illumination microscopy (iSPIM) enables coupled cell identity lineaging and neurodevelopmental imaging in *Caenorhabditis elegans*," *Proc. Natl. Acad. Sci. U. S. A.* **108**(43), 17708–17713 (2011).
10. M. B. Bouchard, V. Voleti, C. S. Mendes, C. Lacefield, W. B. Grueber, R. S. Mann, R. M. Bruno, and E. M. C. Hillman, "Swept confocally-aligned planar excitation (SCAPE) microscopy for high-speed volumetric imaging of behaving organisms," *Nat. Photonics* **9**(2), 113–119 (2015).
11. B. Migliori, M. S. Datta, C. Dupre, M. C. Apak, S. Asano, R. Gao, E. S. Boyden, O. Hermanson, R. Yuste, and R. Tomer, "Light sheet theta microscopy for rapid high-resolution imaging of large biological samples," *BMC Biol.* **16**(1), 57 (2018).
12. T. Chakraborty, M. K. Driscoll, E. Jeffery, M. M. Murphy, P. Roudot, B. Chang, S. Vora, W. M. Wong, C. D. Nielson, H. Zhang, V. Zhemkov, C. Hiremath, E. D. De La Cruz, Y. Yi, I. Bezprozvanny, H. Zhao, R. Tomer, R. Heintzmann, J. P. Meeks, D. K. Marciano, S. J. Morrison, G. Danuser, K. M. Dean, and R. Fiolka, "Light-sheet microscopy of cleared tissues with isotropic, subcellular resolution," *Nat. Methods* **16**(11), 1109–1113 (2019).
13. R. Tomer and K. Deisseroth, "Rapid High-resolution Brain Mapping with CLARITY Optimized Light Sheet Microscopy (COLM)," *Microsc. Microanal.* **21**(S3), 717–718 (2015).
14. R. McGorty, H. Liu, D. Kamiyama, Z. Dong, S. Guo, and B. Huang, "Open-top selective plane illumination microscope for conventionally mounted specimens," *Opt. Express* **23**(12), 16142–16153 (2015).
15. P. Strnad, S. Gunther, J. Reichmann, U. Krzic, B. Balazs, G. de Medeiros, N. Norlin, T. Hirragi, L. Hufnagel, and J. Ellenberg, "Inverted light-sheet microscope for imaging mouse pre-implantation development," *Nat. Methods* **13**(2), 139–142 (2016).
16. A. K. Glaser, N. P. Reder, Y. Chen, C. Yin, L. Wei, S. Kang, L. A. Barner, W. Xie, E. F. McCarty, C. Mao, A. R. Halpern, C. R. Stoltzfus, J. S. Daniels, M. Y. Gerner, P. R. Nicovich, J. C. Vaughan, L. D. True, and J. T. C. Liu, "Multi-immersion open-top light-sheet microscope for high-throughput imaging of cleared tissues," *Nat. Commun.* **10**(1), 2781 (2019).
17. R. McGorty, D. Xie, and B. Huang, "High-NA open-top selective-plane illumination microscopy for biological imaging," *Opt. Express* **25**(15), 17798–17810 (2017).
18. A. Klingberg, A. Hasenberg, I. Ludwig-Portugall, A. Medyukhina, L. Männ, A. Brenzel, D. R. Engel, M. T. Figge, C. Kurts, and M. Gunzer, "Fully automated evaluation of total glomerular number and capillary tuft size in nephritic kidneys using lightsheet microscopy," *J. Am. Soc. Nephrol.* **28**(2), 452–459 (2017).
19. L. A. Barner, A. K. Glaser, L. D. True, N. P. Reder, and J. T. C. Liu, "Solid immersion meniscus lens (SIMlens) for open-top light-sheet microscopy," *Opt. Lett.* **44**(18), 4451–4454 (2019).
20. M. Weber and J. Huisken, "Light sheet microscopy for real-time developmental biology," *Curr. Opin. Genet. Dev.* **21**(5), 566–572 (2011).
21. P. J. Keller, A. D. Schmidt, J. Wittbrodt, and E. H. K. Stelzer, "Digital scanned laser light-sheet fluorescence microscopy (DSLM) of zebrafish and drosophila embryonic development," *Cold Spring Harb. Protoc.* **2011**(10), 1235–1243 (2011).
22. K. Chung, J. Wallace, S. Kim, S. Kalyanasundaram, A. S. Andalman, T. J. Davidson, J. J. Mirzabekov, K. A. Zalocusky, J. Mattis, A. K. Denisin, S. Pak, H. Bernstein, C. Ramakrishnan, L. Grose, V. Gradinaru, and K. Deisseroth, "Structural and molecular interrogation of intact biological systems," *Nature* **497**(7449), 332–337 (2013).
23. E. A. Susaki, K. Tainaka, D. Perrin, H. Yukinaga, A. Kuno, and H. R. Ueda, "Advanced CUBIC protocols for whole-brain and whole-body clearing and imaging," *Nat. Protoc.* **10**(11), 1709–1727 (2015).
24. N. Renier, Z. Wu, D. J. Simon, J. Yang, P. Ariel, and M. Tessier-Lavigne, "IDISCO: A simple, rapid method to immunolabel large tissue samples for volume imaging," *Cell* **159**(4), 896–910 (2014).
25. H. Babcock, *et al.*, "Storm-control," v2019.06.28, Zenodo, doi:10.5281/zenodo.32648572019.
26. B. Balázs, J. Deschamps, M. Albert, J. Ries, and L. Hufnagel, "A real-time compression library for microscopy images," *bioRxiv* (2017).
27. D. Hörl, F. R. Rusak, F. Preusser, P. Tillberg, N. Randel, R. K. Chhetri, A. Cardona, P. J. Keller, H. Harz, H. Leonhardt, M. Treier, and S. Preibisch, "BigStitcher: reconstructing high-resolution image datasets of cleared and expanded samples," *Nat. Methods* **16**(9), 870–874 (2019).

28. M. N. Gurcan, L. Boucheron, A. Can, A. Madabhushi, N. Rajpoot, and B. Yener, "Histopathological Image Analysis: A Review," *IEEE Rev. Biomed. Eng.* **2**, 147–171 (2009).
29. C. Magi-Galluzzi, "Prostate cancer: diagnostic criteria and role of immunohistochemistry," *Mod. Pathol.* **31**(S1), 12–21 (2018).
30. A. H. Scheel, F. Penault-Llorca, W. Hanna, G. Baretton, P. Middel, J. Burchhardt, M. Hofmann, B. Jasani, and J. Rüschoff, "Physical basis of the 'magnification rule' for standardized Immunohistochemical scoring of HER2 in breast and gastric cancer," *Diagn. Pathol.* **13**(1), 19 (2018).
31. T. T. Brunyé, E. Mercan, D. L. Weaver, and J. G. Elmore, "Accuracy is in the Eyes of the Pathologist: The Visual Interpretive Process and Diagnostic Accuracy with Digital Whole Slide Images," *J. Biomed. Inf.* **66**(3), 171–179 (2017).
32. R. Serafin, W. Xie, A. K. Glaser, and J. T. C. Liu, "FalseColor-Python: a rapid intensity-leveling and digital-staining package for fluorescence-based slide-free digital pathology," *PLoS ONE* (in press).
33. M. G. Giacomelli, L. Husvogt, H. Vardeh, B. E. Faulkner-Jones, J. Horneegger, J. L. Connolly, and J. G. Fujimoto, "Virtual hematoxylin and eosin transillumination microscopy using epi-fluorescence imaging," *PLoS One* **11**(8), e0159337 (2016).
34. M. Zhou, J. Li, L. Cheng, L. Egevad, and F.-M. Deng, "Diagnosis of 'poorly formed glands' Gleason pattern 4 prostatic adenocarcinoma on needle biopsy," *Am. J. Surg. Pathol.* **39**(10), 1331–1339 (2015).
35. O. Hassan and A. Matoso, "Clinical significance of subtypes of Gleason pattern 4 prostate cancer," *Transl. Androl. Urol.* **7**(S4), S477–S483 (2018).
36. N. P. Reder, A. K. Glaser, E. F. McCarty, Y. Chen, L. D. True, and J. T. C. Liu, "Open-top light-sheet microscopy image atlas of prostate core needle biopsies," *Arch. Pathol. Lab. Med.* **143**(9), 1069–1075 (2019).
37. C. Dunsby, "Optically sectioned imaging by oblique plane microscopy," *Opt. Express* **16**(25), 20306–20316 (2008).
38. M. Kumar, S. Kishore, J. Nasenbeny, D. L. McLean, and Y. Kozorovitskiy, "Integrated one- and two-photon scanned oblique plane illumination (SOPi) microscopy for rapid volumetric imaging," *Opt. Express* **26**(10), 13027–13041 (2018).
39. M. Levoy, R. Ng, A. Adams, M. Footer, and M. Horowitz, "Light field microscopy," *ACM Trans. Graph.* **25**(3), 924–934 (2006).
40. R. Prevedel, Y. Yoon, M. Hoffmann, N. Pak, G. Wetzstein, S. Kato, T. Schrödel, R. Raskar, M. Zimmer, E. S. Boyden, and A. Vaziri, "Simultaneous whole-animal 3D imaging of neuronal activity using light-field microscopy," *Nat. Methods* **11**(7), 727–730 (2014).
41. G. Zheng, R. Horstmeyer, and C. Yang, "Wide-field, high-resolution Fourier ptychographic microscopy," *Nat. Photonics* **7**(9), 739–745 (2013).
42. K. W. Bishop, A. K. Glaser, and J. T. C. Liu, "Performance tradeoffs for single- and dual-objective open-top light-sheet microscope designs: a simulation-based analysis," *Biomed. Opt. Express* **11**(8), 4627–4650 (2020).